








Tunable exchange bias in the magnetic Weyl semimetal $\text{Co}_3\text{Sn}_2\text{S}_2$

Avia Noah ^{1,*}, Filip Toric,¹ Tomer D. Feld,¹ Gilad Zissman,¹ Alon Gutfreund,¹ Dor Tsruya,¹ T. R. Devidas,¹ Hen Alpern ¹,
Atzmon Vakahi,² Hadar Steinberg ¹, Martin E. Huber ³, James G. Analytis,^{4,5} Snir Gazit ^{1,6},
Ella Lachman ^{4,5} and Yonathan Anahory ¹

¹*Racah Institute of Physics, The Hebrew University, Jerusalem 91904, Israel*

²*Center for Nanoscience and Nanotechnology, Hebrew University of Jerusalem, Jerusalem 91904, Israel*

³*Departments of Physics and Electrical Engineering, University of Colorado Denver, Denver, Colorado 80217, USA*

⁴*Department of Physics, University of California, Berkeley, California 94720, USA*

⁵*Materials Sciences Division, Lawrence Berkeley National Laboratory, Berkeley, California 94720, USA*

⁶*The Fritz Haber Research Center for Molecular Dynamics, The Hebrew University of Jerusalem, Jerusalem 91904, Israel*



(Received 23 December 2020; revised 4 January 2022; accepted 28 March 2022; published 20 April 2022)

Exchange bias is a phenomenon critical to solid-state technologies that require spin valves or nonvolatile magnetic memory. The phenomenon is usually studied in the context of magnetic interfaces between antiferromagnets and ferromagnets, where the exchange field of the former acts as a means to pin the polarization of the latter. In the present study, we report an unusual instance of this phenomenon in the topological Weyl semimetal $\text{Co}_3\text{Sn}_2\text{S}_2$, where the magnetic interfaces associated with domain walls suffice to bias the entire ferromagnetic bulk. Remarkably, our data suggest the presence of a hidden order parameter whose behavior can be independently tuned by applied magnetic fields. For micron-size samples, the domain walls are absent, and the exchange bias vanishes, suggesting the boundaries are a source of pinned uncompensated moment arising from the hidden order. This mechanism suggests that exciting opportunities lie ahead for the application of topological materials in spintronic technologies.

DOI: [10.1103/PhysRevB.105.144423](https://doi.org/10.1103/PhysRevB.105.144423)

I. INTRODUCTION

The phenomenon of exchange bias (EB) was first realized in Co/CoO_x heterostructure particles [1]. The magnetic hysteresis loop of this heterostructure was centered around a field $H_{\text{EB}} = -(H_c^- + H_c^+)/2 \neq 0$, where H_c^+ and H_c^- represent the coercive fields for the positive and negative fields, respectively. The observed shift in the magnetic hysteresis loop was attributed to the pinning of the ferromagnetic (FM) Co moments by the exchange interactions with the antiferromagnetic (AFM) CoO_x . Since then, EB was observed in other heterostructures of different FM and AFM materials [2] including spin glasses [3], superparamagnets [4], and ferrimagnets [5]. Moreover, some realizations of EB can be produced without heterostructures [6,7], and some do not require activation by cooling in a magnetic field and create spontaneous EB that is isothermally set at low temperatures [4,8]. This abundance of systems presenting EB have produced a plethora of suggested mechanisms to explain this phenomenon. The main component of these mechanisms lies in a source of uncompensated spins that induce a preferred direction.

Recently, EB was observed in a pure bulk $\text{Co}_3\text{Sn}_2\text{S}_2$ single crystals [9], with no substrate effects [6] or material doping [7], invoking the need for a different mechanism for the EB they present. $\text{Co}_3\text{Sn}_2\text{S}_2$ was recently discovered as a mag-

netic Weyl semimetal, where the breaking of time-reversal symmetry due to ferromagnetism satisfies the requirement of a broken symmetry to create the topological band structure [10–18]. Of particular interest is the nontrivial interplay between strong magnetic correlations and the emergent topological band structure of Weyl fermions in such materials [19–25], which is not present in their inversion-symmetry-breaking counterparts. Specifically, the magnetic moments in $\text{Co}_3\text{Sn}_2\text{S}_2$ reside on the Co sites and are arranged in a layered kagome lattice. Experimentally, below 175 K, a dominant FM phase with an easy axis oriented out of the kagome plane is observed, although this phase may coexist with an in-plane (IP) antiferromagnetic phase [9,21]. Below this temperature, the electronic dispersion has been shown to host Weyl fermions [16,26] associated with a giant anomalous Hall effect [12,13,27].

Even at the level of basic magnetic properties, experimental observations display puzzling inconsistencies. Explicitly, the reported values of magnetic saturation field H_s range 0.06–0.5 T in the bulk [9,12,13,21,26,28–30], and may reach values of a few T in micron-size samples [31–35]. Such large variations are surprising since H_s is a material property determined by the crystalline structure and electronic orbitals, and the large variability is unlikely to be due to a simple geometrical factor or sample quality. Presently, these unusual magnetic properties including the presence of EB and their underlying physics are far from understood.

In this work, we address these questions by using a combination of transport measurements and magnetic imaging to

*avia.noah@mail.huji.ac.il

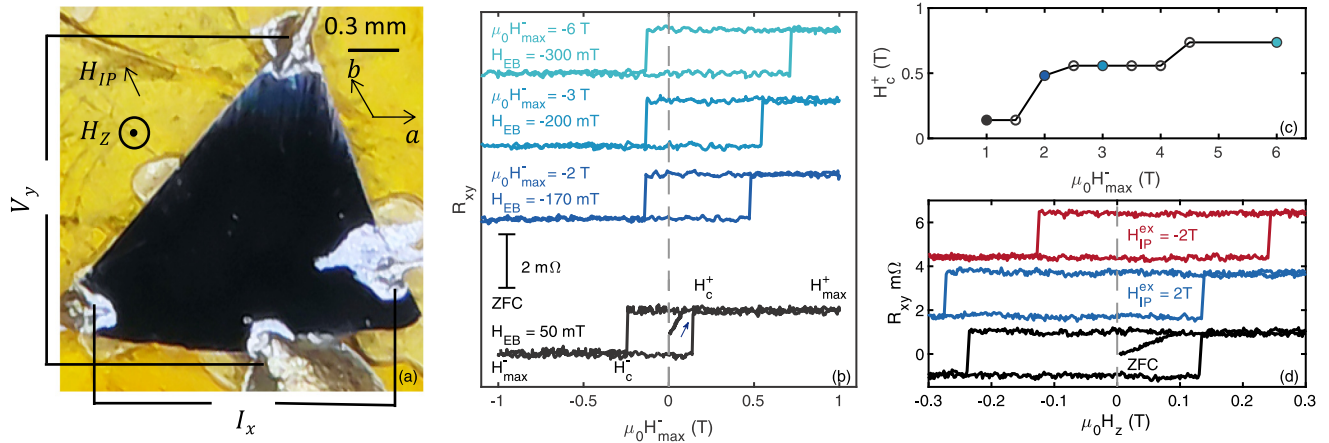


FIG. 1. Controlling the exchange bias of $\text{Co}_3\text{Sn}_2\text{S}_2$ single crystal sample by applying out-of-plane and in-plane field protocols at 4.2 K. (a) Optical image of the sample and a schematic depicting paths for current I_x , voltage probe V_y , and the crystal axes. (b) Hall resistance $R_{xy} = V_y/I_x$ as a function of the out-of-plane field $\mu_0 H_z$. After ZFC the field is swept between ± 1 T resulting in a rectangular R_{xy} with $H_{EB} = 50$ mT (black). Controlling the positive coercive field H_c^+ by performing a larger field excursion in the negative direction $\mu_0 H_{\max}^- = -2, -3, -6$ T while keeping $\mu_0 H_{\max}^+ = 1$ T resulting in $H_{EB} = -170, -200, -300$ mT, respectively (dark blue to light blue). (c) H_c^+ as a function of $\mu_0 H_{\max}^-$, with colored dots corresponding to the measurements shown in (b). (d) Each measurement is performed at $H_{IP} = 0$ after ZFC (black), after an excursion to $H_{IP}^{\text{ex}} = 2$ T resulting in $H_c^+ = 139$ mT and $H_c^- = -275$ mT, $H_{EB} = 68$ mT (blue), and to $\mu_0 H_{IP}^{\text{ex}} = -2$ T yielding $H_c^+ = 244$ mT, $H_c^- = -128$ mT, and $H_{EB} = -58$ mT (red). Three loops performed for each measurement gave similar results, and one representative result is shown for clarity. In both (b) and (d) the curves for different protocols are shifted vertically for clarity.

visualize the magnetic domains and elucidate the mechanism underlying the EB in $\text{Co}_3\text{Sn}_2\text{S}_2$. We reveal a tunable EB, that can be set and changed isothermally at low temperatures. We attribute this tunability to a hidden IP magnetic order that is likely related to the domain walls. These findings suggest a promising future for the application of magnetic Weyl semimetals in memory and spintronic technologies, although they may require further miniaturization for practical applications.

II. RESULTS

$\text{Co}_3\text{Sn}_2\text{S}_2$ crystals were grown by the self-flux method commonly used for these crystals [9,36,37]. For electrical transport measurements, four aluminum wires were glued to an 80- μm -thick sample using silver epoxy, as shown in Fig. 1(a) (see the Methods section and Supplemental Material Note 6 [38]). The sample was zero-field cooled (ZFC) down to 4.2 K, where the sample displays FM characteristics [21]. A 2-mA current was applied along the x axis while the voltage V_y was measured along the y axis [see Fig. 1(a)]. We report the Hall resistance $R_{xy} = V_y/I_x$ as a function of the out-of-plane (OOP) magnetic field $\mu_0 H_z$ under distinct magnetic field protocols up to 6 T.

As an example, Fig. 1(b) (black curve) presents R_{xy} measurements starting from ZFC and ramping H_z at a rate of 4 mT/s to +1 T. Subsequently, we carried out a full -1 - to $+1$ -T magnetic field loop. During the initial field ramp, R_{xy} grows smoothly, starting from zero and reaching saturation at 95 mT [see Fig. 3(b) blue curve]. The following R_{xy} curve exhibits sharp jumps associated with two distinct coercive fields, $H_c^+ = 140$ mT and $H_c^- = -240$ mT, for positive and negative H_z , respectively [Fig. 1(b), black curve]. The asymmetry between the coercive fields yields $H_{EB} = 50$ mT. We

note that these H_c^\pm values are reproducible within our experimental resolution (better than 5 mT), as long as the field is swept symmetrically from +1 T to -1 T ($\mu_0 |H_{\max}^\pm| = 1$ T). As previously [9] reported for ZFC conditions, the lower coercive field is determined by the direction of the first field excursion. Here the positive direction was chosen initially, and we obtain $|H_c^+| < |H_c^-|$, and thus $H_{EB} > 0$.

Our results differ from those in previous reports, which did not observe a finite H_{EB} when performing a magnetization loop with a much larger $\mu_0 H_{\max}^\pm \sim 9$ T. It is therefore interesting to explore the evolution of the hysteresis loop at intermediate fields, and for asymmetric field-sweep protocols. With that goal in mind, we apply such a protocol with $\mu_0 H_{\max}^- = -2, -3, -6$ T while fixing $\mu_0 H_{\max}^+ = 1$ T [Fig. 1(b) blue curves]. Interestingly, we find that H_c^+ values increase by more than a factor of 5, ranging from 140 mT ($\mu_0 H_{\max}^- = -1$ T) to 736 mT ($\mu_0 H_{\max}^- = -6$ T). In contrast, H_c^- varies only slightly from the -240 mT observed in the ± 1 -T symmetric sweep to -140 mT for all the other sweeps. Consequently, over these protocols, H_{EB} changes both sign and magnitude from $H_{EB} = 50$ mT after ZFC to -300 mT after $\mu_0 H_{\max}^- = -6$ T. Different values of $|H_{\max}^\pm|$ yield different values of H_c^\mp [Fig. 1(c)]. Curiously, H_c^+ is constant for distinct values of H_{\max}^- resulting in a plateau structure as shown in Fig. 1(c). The reverse protocol, i.e., keeping $H_{\max}^- = -1$ T and varying H_{\max}^+ shows similar results that are detailed in Supplemental Material Note 2 and Supplemental Material Fig. 2 [38]. The observed sign reversibility in H_{EB} implies that it can be set to be vanishingly small, as demonstrated in Supplemental Material Note 3 [38].

It is essential to contrast the above result with those from minor loop protocols used in conventional ferromagnets, where distinct H_c values can be reached by applying $|H_{\max}| < H_s$. Physically, this phenomenon can be attributed

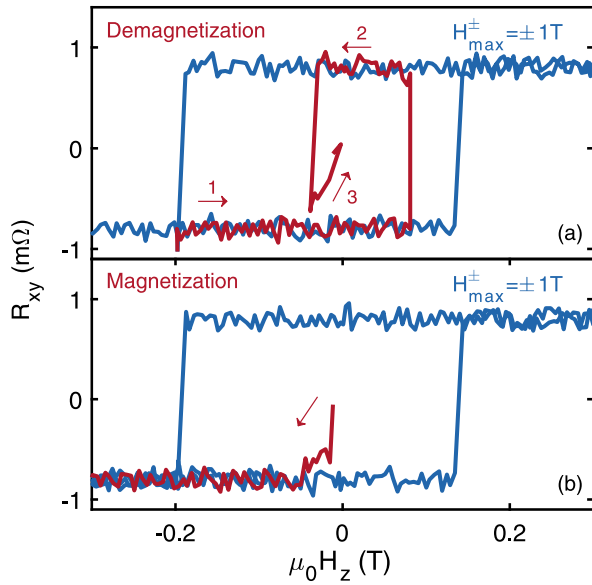


FIG. 2. Demagnetization and magnetization. (a) Demagnetization protocol, the field swept from -1 to 1 T to initialize the sample and from $+1$ until H_c^- is reached (blue). Sweeping the field between the distinct H_c^\pm after three repetitions produces a vanishingly small R_{xy} (red). (b) Magnetization of the sample. The field is first swept to -1 T (red) and then a $+/-1$ -T loop is performed (blue).

to residual magnetic domains that are antiparallel with the external field [39–42]. The present case is different, since $|H_{\max}| > H_s$ in all the protocols described above. Our measured H_s is in good agreement with previous reports where $H_s \lesssim 500$ mT [9,12,13,21,28–30].

The nontrivial evolution of H_c^\pm as a function of $|H_{\max}|$ beyond H_s indicates that H_c^\pm does *not* depend solely on OOP magnetization. Notably, previous reports could not rule out a slight canting of magnetic moments below 125 K, even though the magnetization was predominantly oriented OOP [12,21]. Moreover, theoretical calculations predict that even slight canting might dramatically affect the Weyl nodes [19] and associated magnetic textures [20]. Motivated by these theoretical predictions, it is also interesting to study the effect of an IP field, H_{IP} , on H_c^\pm .

To reveal the influence of H_{IP} on H_c^\pm , we conduct IP field excursions $H_{\text{IP}}^{\text{ex}} = \pm 2$ T, followed by the $\mu_0 |H_{\max}^\pm| = 1$ T loop protocol at $H_{\text{IP}} = 0$. Considering that the IP saturation field is 23 T and given that the IP magnetization varies linearly [29] from 0° for $H_{\text{IP}} = 0$ to 90° for $H_{\text{IP}} = 23$ T we deduce that our field excursion causes a tilt of $\sim 8^\circ$. We start by measuring R_{xy} after ZFC, before applying any IP field. Under these conditions, $R_{xy}(H_z)$ shows the expected $H_c^+ = 128$ mT and $H_c^- = -241$ mT with $H_{\text{EB}} = 56$ mT [black line, Fig. 1(d)]. An IP field is applied reaching $\mu_0 H_{\text{IP}}^{\text{ex}} = 2$ T and then ramped down to zero before measuring again $R_{xy}(H_z)$. The $R_{xy}(H_z)$ curve reveals a small increase in both $H_c^+ = 139$ mT, $H_c^- = -275$ mT and $H_{\text{EB}} = 68$ mT (blue line) with respect to the ZFC measurements. On the other hand, applying an IP field excursion in the other direction up to $\mu_0 H_{\text{IP}}^{\text{ex}} = -2$ T and back to zero results in a change of sign in H_{EB} , with $H_c^+ = 244$ mT, $H_c^- = -128$ mT, and $H_{\text{EB}} = -58$ mT (red

line). This experimental observation indicates that even a small degree of canting has a dramatic effect on H_{EB} . We emphasize that the material retains a memory of the H_{EB} magnitude and sign, even after the IP field is set to zero. We also note that no hysteresis behavior is observed for the IP magnetization as a function of the IP field [12,29].

In order to further explore the possibility that the H_{EB} information is not encoded in the OOP magnetization, we now attempt to demagnetize the sample, using a minor loop protocol. Explicitly, we carry out one minor loop sweep with $\mu_0 |H_{\max}^\pm| \sim H_c^\pm$ [Fig. 2(a), red curves number 1 and 2]. The results reveal a vanishingly small R_{xy} (number 3), which naively indicates that the sample is demagnetized. *A priori*, one would expect a demagnetized sample to lose all H_{EB} information and return to the initial random ZFC conditions. To test this expectation, we carry out an OOP field excursion oppositely aligned with the initial ZFC excursion (namely, we sweep toward negative fields). Remarkably, we find precisely the same hysteresis loop as after the ZFC loop [Fig. 2(b), blue curve]. This finding suggests that even though the sample appears demagnetized in transport, it retains the information regarding the direction of the first field excursion after ZFC. More broadly, this provides experimental evidence that H_{EB} information is stored in degrees of freedom other than the global OOP magnetization.

To gain a better insight into the magnetic structure, we conduct local magnetic field imaging $B_z(x, y)$ using a scanning superconducting quantum interference device (SQUID) that resides at the end of a sharp tip [Fig. 3(a)]. The SQUID-on-tip (SOT) provides high spatial resolution for magnetic imaging [43,44] reaching single-spin sensitivity [45,46]. Images are taken at 4.2 K with SQUIDs having a diameter ranging 110–130 nm (see the Methods section and Supplemental Material Note 1 [38]).

Figure 3(c) presents the results of imaging the ZFC sample with magnetic features of a few microns yielding a magnetic contrast of ~ 50 mT. With increasing field, domains parallel to the field grow at the expense of the antiparallel domains [Figs. 3(c)–3(f) and Movie 1 in the Supplemental Material [38]]. Above the saturation field, 95 mT, starting from ZFC conditions, the magnetic contrast drops below 1.5 mT. The local magnetic structure does not appear to further evolve on this scale, which is in agreement with transport and global magnetization measurements [9,12,13,21,28–30]. These small micron-sized magnetic features were not observed in previous magnetic imaging work done on this material [47,48] most likely because the authors did not image the sample in ZFC conditions.

As shown previously, while the ZFC and the demagnetized state both exhibit a vanishing R_{xy} [Figs. 2 and 3(b), green curve], there is a crucial difference between these states in that the latter retains the H_{EB} memory, while the former does not. It is therefore interesting to observe whether this difference is also apparent in the local magnetic structure. To examine this, we compare the respective magnetic structures of the two states [Figs. 3(g)–3(j) and Supplemental Material Movie 2 [38]]. The results indicate that, unlike the ZFC state, the demagnetized state exhibits a stripe pattern with a typical width of 10 μm , and a length that extends beyond our field of view (45 μm). The memory of

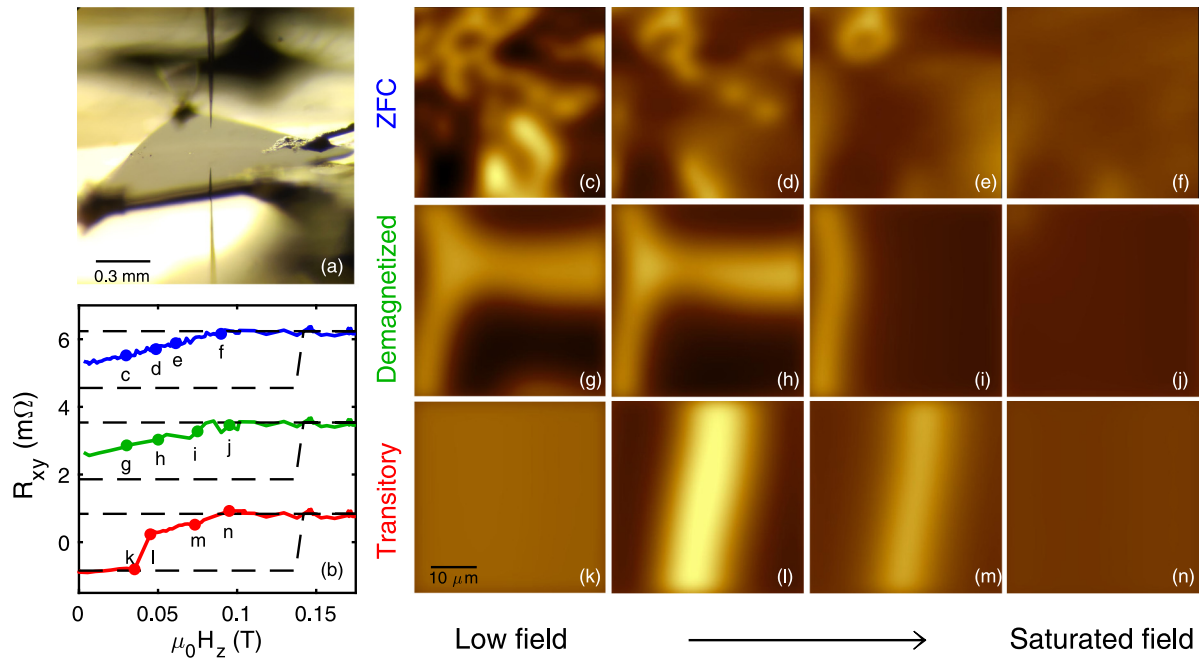


FIG. 3. Scanning SOT microscopy images of $\text{Co}_3\text{Sn}_2\text{S}_2$ bulk at 4.2 K. (a) Optical image of the SOT pointing down, the sample, and the reflection of the SOT on the sample. (b) R_{xy} as a function of applied magnetic field for different phases of the sample. ZFC to saturated field (blue), demagnetized state to saturated field (green), and magnetization reversal with transitory state (red). R_{xy} corresponding to a loop with $\mu_0 |H_{\max}^\pm| = 1$ T is shown for comparison (black dashed). The fields at which the images were taken are marked with dots. The curves for different protocols are shifted vertically for clarity. (c)–(n) Sequence of magnetic images of different states of the sample at distinct values of applied out-of-plane field $\mu_0 H_z$. (c)–(f). Evolution from ZFC to the saturation field. $\mu_0 H_z = 45$ mT (c), $\mu_0 H_z = 65$ mT (d), $\mu_0 H_z = 85$ mT (e), $\mu_0 H_z = 95$ mT (f). (g)–(j) Evolution of demagnetization to the saturation field. $\mu_0 H_z = 30$ mT (g), $\mu_0 H_z = 50$ mT (h), $\mu_0 H_z = 75$ mT (i), $\mu_0 H_z = 95$ mT (j). (k)–(n) Magnetization reversal with transitory state. $\mu_0 H_z = 35$ mT (k), $\mu_0 H_z = 45$ mT (l), $\mu_0 H_z = 75$ mT (m), $\mu_0 H_z = 95$ mT (n). All images are $45 \times 45 \mu\text{m}^2$, pixel size 480 nm (c)–(f) and 980 nm (g)–(n), acquisition time 8 min/image (c)–(f) and 5.8 min/image (g)–(n). The bright to dark color scale represents 50 mT and is the same for all images. See Supplemental Material Movies 1–3 corresponding to images (c)–(f), (g)–(j), (k)–(n), respectively.

a finite exchange bias H_{EB} is retained only by the larger domain.

Similar magnetic domain structures are observed when the magnetization reverses [Figs. 3(k)–3(n) and Movie 3] [38]. We also note that similar domains of typical size of a few tens of microns were recently observed by MFM and by scanning Kerr microscopy in similar conditions [47,48]. Notably, the appearance of these features always coincides precisely with a sign change in R_{xy} [Fig. 3(b), red curve], indicating that our microscopic images ($45 \times 45 \mu\text{m}^2$) are representative of the much larger sample (mm size). We note that this transitory state is observed only for loops where $|H_{\max}^\pm|$ is relatively low $|H_{\max}^\pm| < 300$ mT, and is only visible for less than 30 mT beyond the field at which R_{xy} changes sign. For protocols with a larger $|H_{\max}^\pm|$, no transitory state was observed and instead an abrupt change in local magnetic field was recorded by the SOT between two field steps (smaller than 5 mT) coinciding with the change of sign of R_{xy} . This indicates that the magnetization reversal in such a case occurs abruptly throughout the sample with no evolution of the magnetic landscape observed on either side of the magnetic transition.

From the above observations, we can conjecture that there is a minimal length scale of the domains required for the appearance of EB. This hypothesis can be tested by repeating the same field sweep protocols on samples with lateral dimensions of a few tens of microns, which is comparable to the

size of the domains following the initial field sweep [$\approx 45 \mu\text{m}$, Figs. 3(g)–3(n)]. For such samples, we expect to see a single or at most a few magnetic domains. We use a focused ion beam (FIB), to cut a slab of area of $60 \times 30 \mu\text{m}^2$ from the bulk crystal with thicknesses ranging 1–42 μm and the c axis pointing out of the plane [Fig. 4(a)]. Platinum is then used as a contact to lithographically defined 50-nm-thick Nb tracks to the sample. Chemical analysis reveals that the sample maintained a stoichiometric ratio of its constituent elements except near the surface where C and Ga were detected (Supplemental Material Note 6 [38]). The FIB sample is ZFC only down to 10 K in order to avoid the complications arising from the superconductivity in Nb ($T_c < 9.2$ K). Currents ranging 0.4–0.8 mA are applied while the transverse voltage is measured as shown in Fig. 4(b), maintaining similar current densities as in the bulk measurements.

The results of these experiments for a 6- μm -thick sample are shown in Figs. 4(c) and 4(d). First, we note that the H_{EB} resulting from a complete $\mu_0 |H_{\max}| = H_c$ loop protocol is vanishingly small ($H_{\text{EB}} < 5$ mT). Second, starting from ZFC conditions (blue curve), we find that $H_c > 1$ T. This value should be compared with the $H_c \sim 0.2$ T that was previously obtained with an identical protocol on mm-sized samples. We find that the H_c values are remarkably robust to radically different protocols. In particular, we did not observe demagnetization [Fig. 4(c)] or variation in H_c under the application of

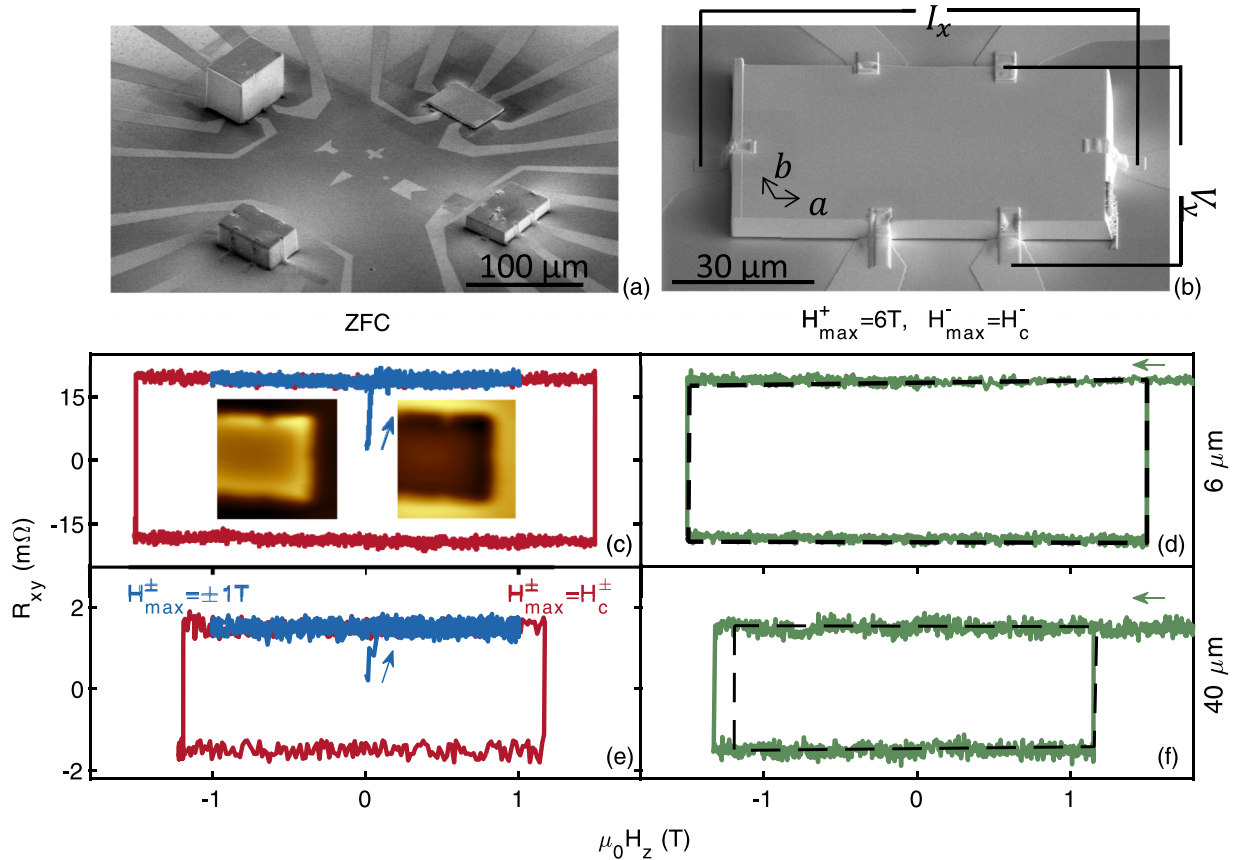


FIG. 4. R_{xy} measurements of $\text{Co}_3\text{Sn}_2\text{S}_2$ FIB samples with distinct thicknesses ranging 6–42 μm at 10 K. (a) SEM image of four different $\text{Co}_3\text{Sn}_2\text{S}_2$ single crystals cut by FIB with an area of $60 \times 30 \mu\text{m}^2$ and thicknesses ranging 6–42 μm . (b) SEM image at higher magnification of the 6- μm -thick sample including a schematic of the measurement and the crystal axes. (c)–(f) R_{xy} measurements under different out-of-plane protocols. (c),(d) Sample thickness 6 μm . (e),(f) Sample thickness 42 μm . (c),(e) Blue: After ZFC, the field is swept three times between ± 1 T. Red: Finding the positive and negative coercive fields. Sweeping the field six times between the positive and negative coercive fields does not change the coercive field, therefore no demagnetization process is possible in the FIB sample. Only two curves are shown for clarity. (d),(f) Applying a positive 6-T field and then sweeping the field until the negative coercive field does not change the coercive field of the 6- μm sample. The negative coercive field of the 42- μm sample grows by 200 mT resulting in $H_{\text{EB}} = 100$ mT. The R_{xy} measurements of samples with other thickness are presented in Supplemental Material Movie 4 [38]. (c) Inset: SOT imaging of the 6- μm sample before and after H_c^+ presenting a single domain structure which flips at H_c^+ . All images are $45 \times 45 \mu\text{m}^2$, pixel size 480 nm, acquisition time 9 min/image. The bright to dark color scale represents 10 mT and is the same for all images. See Supplemental Material Movie 8 [38].

$\mu_0 H_z = 6$ T [Fig. 4(d)]. We further corroborate the absence of magnetic domain walls via SOT microscopy. The entire portion of the sample that was probed (more than 50% of the area) changed magnetization abruptly in coincidence with the jump in R_{xy} [Fig. 4(c) insets, Supplemental Material Movie 8 [38]]. This observation provides strong experimental evidence for the presence of a single sample-sized magnetic domain. These large values of H_c are similar to those previously reported in recent works [31–34].

Results from applying the same analysis to samples with different thicknesses (Supplemental Material Movie 4 [38]), revealed only a small, or no clear dependence of H_c on the sample thickness. In addition, the demagnetization protocol has no effect on H_c for any of the thicknesses tested. Finally, in all but the thickest (42 μm) sample we did not detect any measurable EB [Figs. 4(e) and 4(f)]. The fact that the thickest microcrystal showed some EB suggests that the lateral dimensions are near the critical dimensions to obtain EB (few tens of microns). A summary of H_{EB} , H_c^{max} , and R_{xy}

measured for all the samples presented in this work is shown in Fig. S7 [38].

III. DISCUSSION

We now turn to discuss the physical consequences of our experimental findings. It is clear that H_{EB} is *not* a static material property and can be tuned by applying IP and OOP field protocols. That H_c^\pm evolves with H_{max}^\mp well beyond the saturation field implies an undetectable evolution in the spin texture, which dramatically affects H_c of the entire sample. The fact that the sign of H_{EB} is determined by the direction of the IP field, even after that field is no longer applied, provides experimental evidence that IP spin canting determines the exchange bias of the OOP magnetic moment in both sign and size.

In contrast, for microcrystals thinner than 40 μm , we measure a vanishingly small H_{EB} and the values of H_c^\pm were found to be independent of the applied magnetic field protocol.

The measured values of H_c^\pm were also more than five times larger than the H_c^\pm measured for the mm-sized sample using a $H_{\max}^\pm = 1$ T protocol (see Fig. S7 [38]). Looking at the thickest measured microcrystal, we note the appearance of a finite $H_{\text{EB}} = 10$ mT and a measurable drop in H_c^\pm . Our magnetic imaging results show that domain walls are not formed in microcrystals [Fig. 4(c) and Movie 8 [38]]. The correlation between the magnitude of H_c^\pm and the presence of finite H_{EB} is yet to be formally explained, however, the fact that they both depend on the sample size on length scales that fit the domain size (few tens of microns) suggest that the presence of the domain wall is one of the plausible explanations. Broadly, a finite EB entails the presence of uncompensated moments. Indeed, for larger H_c , these moments are more susceptible to polarization and hence their contribution to the EB will be diminished.

Although the precise mechanism for the EB in this material remains to be identified, previous reports combined with our present findings may point to a possible physical mechanism. A good candidate should be an uncompensated spin texture such as an AFM phase that would coexist with the dominating FM order. At the domain walls, ferromagnetism is weak and permits the appearance of competing magnetic orders. In that regard, Ref. [21] reported that the coexistence of AFM and FM survives all the way down to 25 K, in proximity to the saturation field where the presence of domain walls is expected. Our results show that these domain walls are only stable enough to be measured for protocols where $H_{\max}^\pm < 0.3$ T (transitory state Fig. 3). The authors of Ref. [21] used a protocol with $H_{\max}^\pm = \pm 6$ T. We speculate that this is the reason why they did not observe the AFM phase down to 4.2 K. The AFM state presents a chiral magnetic structure of the IP spin component that could be caused by the inherent magnetic frustration of kagome lattice or Dzyaloshinsky-Moriya (DM) interlayer interaction. The two possible chiralities of the IP AFM state could be toggled by an IP field and affect H_c . Moreover, it is interesting to relate these results to other ferromagnets exhibiting exchange bias due to interlayer DM interaction [49] which are allowed by symmetry in $\text{Co}_3\text{Sn}_2\text{S}_2$. These results could also be related to the memory effect emerging from the chiral domains in an in-plane AFM kagome [50]. It is worth noting that DM interaction is allowed by symmetry argument since the inversion centers present in $\text{Co}_3\text{Sn}_2\text{S}_2$ are not located at the bisecting point of the straight line between two out-of-plane Co atoms [51]. The experimental evidence in favor of local AFM order is only circumstantial and invites future explorations, which will allow for direct confirmation of this scenario or an equally interesting alternative.

Another tantalizing mechanism involves electronic boundary states that were theoretically predicted to form at the interface between two magnetic domains in magnetic Weyl semimetals. While an electronic mechanism is less likely to drive the reported EB phenomena, our work provides a concrete protocol for nucleating magnetic domain walls that are essential for the observation of topological boundary effects in magnetic Weyl semimetals. The presence of magnetic boundaries encompass exciting transport and electrostatic phenomena related to the axial magnetic field [20,22]

that inspired recent experimental efforts [22,24,25]. Though beyond the scope of the current work, our experimental system provides a unique opportunity to address these exotic phenomena present at magnetic domain walls.

IV. METHODS

A. Single crystal growth

Single crystals were grown from a stoichiometric ratio of elements using the self-flux method (Sn flux). The elements were placed in an AlO_x crucible and sealed in an evacuated quartz tube.

B. Transport measurements

Transport measurements were performed at 4.2 K cooling inside a liquid helium dewar. Unless otherwise mentioned, a current of 2 mA was applied along the *ab* plane. The distance between current contacts was 1.6 mm and between V_y contacts 1.2 mm. In all measurements, 25 μm Al wires were glued using silver epoxy to an 80- μm -thick sample as measured using a three-dimensional (3D) profilometer. In bulk samples, each transport data set was measured after ZFC to initialize the sample. A vector magnet was used to apply IP and OOP magnetic fields. The magnet consists of a standard coil for OOP field and a split coil of IP field.

C. Scanning SQUID-on-Tip microscopy

The SOT was fabricated using self-aligned three-step thermal deposition of Pb at cryogenic temperatures, as described previously [45]. Supplemental Material Fig. S1 [38] shows the measured quantum interference pattern of one of the SOTs used for this work with an effective diameter of 130 nm and a maximum critical current of 98 μA . The asymmetric structure of the SOT gives rise to a shift of the interference pattern resulting in good sensitivity in a wide range of fields. All measurements were performed at 4.2 K in a low pressure He of ~ 1 mbar.

D. Statistic and uncertainties

Statistic and uncertainties: The resolution of the magnetic field is 4 mT and is determined by the magnetic sweep rate (4 mT/s) and the integration time of the signal (1 s). A systematic error on the magnetic field of a few G at most can be attributed to trapped flux in the magnet and the residual magnetization of surrounding parts. Typically, we did not observe drifts of H_c larger than our field resolution (4 mT) for identical protocols on a given sample. The uncertainty on V_{xy} is dominated by electrical noise. A usual systematic DC offset was observed and removed by symmetrizing the data around $V_{xy} = 0$. The uncertainty on V_{xy} is the main source of uncertainty of R_{xy} . The uncertainty on the distance is better than the last digit displayed. The SOT images are slightly distorted due to the piezoelectric hysteresis estimated to be 10–20%.

ACKNOWLEDGMENTS

We would like to thank B. Yan, Z. Ovadyahu, A. Vaknin, and A. Capua for fruitful discussions. We would like to thank S. Ben Atar for manufacturing the SOT microscope, N. Katz for growing the Nb thin films, and to E. Sabag which who was responsible for the construction of the Quantum Imaging Lab. This work was supported by European Research Council (ERC) Foundation Grant No. 802952 and Israel Science Foundation (ISF) Grants No. 649/17 and No. 2178/17. The international collaboration on this work was fostered by the EU-COST Action CA16218. S. G. acknowledges support from Israel Science Foundation Grant No. 1686/18. H.S. acknowledges funding provided by DFG Priority program Grant 443404566 and Israel Science Foundation Grant 861/19. J.G.A. and E.L. acknowledges support from the Gordon and Betty Moore Foundation's EPiQS Initiative through Grant No. GBMF9067 and National Science Foundation un-

der Grant No. 1905397. E.L. is an awardee of the Weizmann Institute of Science - National Postdoctoral Award Program for Advancing Women in Science. F. T. is an awardee of the Hebrew University Center for Nanoscience and Nanotechnology Postdoctoral Fellowship.

Y.A., E.L., A.N., and S.G. conceived the experiment and analyzed the data. A.N. and Y.A. performed the scanning SOT measurements and the transport measurements. A.N., T.D.F., F.T., G.Z., and Y.A. constructed the scanning SOT microscope. A.N., F.T., T.D.F., G.Z., A.G., D.T., and Y.A. fabricated and characterized the SOT devices. M.E.H. developed the SOT readout system. E.L. and J.G.A. grew the crystals. A.V., Y.A., A.N., G.Z., A.G., and H.A. fabricated and measured the FIB samples. A.N., T.R.D., and H.S. performed the in-plane transport measurements. Y.A., S.G., A.N., E.L., F.T., and J.G.A. wrote the paper with contributions from all authors.

-
- [1] W. H. Meiklejohn and C. P. Bean, New magnetic anisotropy, *Phys. Rev.* **105**, 904 (1957).
- [2] Y. Guang, I. Bykova, Y. Liu, G. Yu, E. Goering, M. Weigand, J. Gräfe, S. K. Kim, J. Zhang, H. Zhang, Z. Yan, C. Wan, J. Feng, X. Wang, C. Guo, H. Wei, Y. Peng, Y. Tserkovnyak, X. Han, and G. Schütz, Creating zero-field skyrmions in exchange-biased multilayers through x-ray illumination, *Nat. Commun.* **11**, 949 (2020).
- [3] M. Ali, P. Adie, C. H. Marrows, D. Greig, B. J. Hickey, and R. L. Stamps, Exchange bias using a spin glass, *Nat. Mater.* **6**, 70 (2007).
- [4] B. M. Wang, Y. Liu, P. Ren, B. Xia, K. B. Ruan, J. B. Yi, J. Ding, X. G. Li, and L. Wang, Large Exchange Bias After Zero-Field Cooling from an Unmagnetized State, *Phys. Rev. Lett.* **106**, 077203 (2011).
- [5] F. Canet, S. Mangin, C. Bellouard, and M. Piecuch, Positive exchange bias in ferromagnetic-ferrimagnetic bilayers: FeSn/FeGd, *Europhys. Lett.* **52**, 594 (2000).
- [6] K. G. West, D. N. H. H. Nam, J. W. Lu, N. D. Bassim, Y. N. Picard, R. M. Stroud, and S. A. Wolf, Exchange bias in a single phase ferrimagnet, *J. Appl. Phys.* **107**, 113915 (2010).
- [7] A. K. Nayak, M. Nicklas, S. Chadov, P. Khuntia, C. Shekhar, A. Kalache, M. Baenitz, Y. Skourski, V. K. Guduru, A. Puri, U. Zeitler, J. M. D. Coey, and C. Felser, Design of compensated ferrimagnetic heusler alloys for giant tunable exchange bias, *Nat. Mater.* **14**, 679 (2015).
- [8] A. Migliorini, B. Kuerbanjiang, T. Huminiuc, D. Kepaptsoglou, M. Muñoz, J. L. F. Cuñado, J. Camarero, C. Aroca, G. Vallejo-Fernández, V. K. Lazarov, and J. L. Prieto, Spontaneous exchange bias formation driven by a structural phase transition in the antiferromagnetic material, *Nat. Mater.* **17**, 28 (2018).
- [9] E. Lachman, R. A. Murphy, N. Maksimovic, R. Kealhofer, S. Haley, R. D. McDonald, J. R. Long, and J. G. Analytis, Exchange biased anomalous hall effect driven by frustration in a magnetic kagome lattice, *Nat. Commun.* **11**, 560 (2020).
- [10] M. Hirschberger, S. Kushwaha, Z. Wang, Q. Gibson, S. Liang, C. A. Belvin, B. A. Bernevig, R. J. Cava, and N. P. Ong, The chiral anomaly and thermopower of weyl fermions in the Half-Heusler GdPtBi, *Nat. Mater.* **15**, 1161 (2016).
- [11] K. Kuroda, T. Tomita, M. T. Suzuki, C. Bareille, A. A. Nugroho, P. Goswami, M. Ochi, M. Ikhlas, M. Nakayama, S. Akebi, R. Noguchi, R. Ishii, N. Inami, K. Ono, H. Kumigashira, A. Varykhalov, T. Muro, T. Koretsune, R. Arita, S. Shin, T. Kondo, and S. Nakatsuji, Evidence for magnetic weyl fermions in a correlated metal, *Nat. Mater.* **16**, 1090 (2017).
- [12] E. Liu, Y. Sun, N. Kumar, L. Muechler, A. Sun, L. Jiao, S. Y. Yang, D. Liu, A. Liang, Q. Xu, J. Kroder, V. Süß, H. Borrmann, C. Shekhar, Z. Wang, C. Xi, W. Wang, W. Schnelle, S. Wirth, Y. Chen, S. T. B. Goennenwein, and C. Felser, Giant anomalous hall effect in a ferromagnetic kagome-lattice semimetal, *Nat. Phys.* **14**, 1125 (2018).
- [13] Q. Wang, Y. Xu, R. Lou, Z. Liu, M. Li, Y. Huang, D. Shen, H. Weng, S. Wang, and H. Lei, Large intrinsic anomalous hall effect in half-metallic ferromagnet $\text{Co}_3\text{Sn}_2\text{S}_2$ with magnetic weyl fermions, *Nat. Commun.* **9**, 3681 (2018).
- [14] A. Sakai, Y. P. Mizuta, A. A. Nugroho, R. Sihombing, T. Koretsune, M. T. Suzuki, N. Takemori, R. Ishii, D. Nishio-Hamane, R. Arita, P. Goswami, and S. Nakatsuji, Giant anomalous nernst effect and quantum-critical scaling in a ferromagnetic semimetal, *Nat. Phys.* **14**, 1119 (2018).
- [15] L. Ye, M. Kang, J. Liu, F. von Cube, C. R. Wicker, T. Suzuki, C. Jozwiak, A. Bostwick, E. Rotenberg, D. C. Bell, L. Fu, R. Comin, and J. G. Checkelsky, Massive dirac fermions in a ferromagnetic kagome metal, *Nature (London)* **555**, 638 (2018).
- [16] N. Morali, R. Batabyal, P. K. Nag, E. Liu, Q. Xu, Y. Sun, B. Yan, C. Felser, N. Avraham, and H. Beidenkopf, Fermi-arc diversity on surface terminations of the magnetic weyl semimetal $\text{Co}_3\text{Sn}_2\text{S}_2$, *Science* **365**, 1286 (2019).
- [17] J.-X. Yin, S. S. Zhang, G. Chang, Q. Wang, S. S. Tsirkin, Z. Guguchia, B. Lian, H. Zhou, K. Jiang, I. Belopolski, N. Shumiya, D. Multer, M. Litskevich, T. A. Cochran, H. Lin, Z. Wang, T. Neupert, S. Jia, H. Lei, and M. Z. Hasan, Negative flat band magnetism in a spin-orbit-coupled correlated kagome magnet, *Nat. Phys.* **15**, 443 (2019).
- [18] Y. Xu, J. Zhao, C. Yi, Q. Wang, Q. Yin, Y. Wang, X. Hu, L. Wang, E. Liu, G. Xu, L. Lu, A. A. Soluyanov, H. Lei, Y. Shi, J. Luo, and Z.-G. Chen, Electronic correlations and flattened

- band in magnetic weyl semimetal candidate $\text{Co}_3\text{Sn}_2\text{S}_2$, *Nat. Commun.* **11**, 3985 (2020).
- [19] M. P. Ghimire, J. I. Facio, J.-S. You, L. Ye, J. G. Checkelsky, S. Fang, E. Kaxiras, M. Richter, and J. van den Brink, Creating weyl nodes and controlling their energy by magnetization rotation, *Phys. Rev. Research* **1**, 032044(R) (2019).
- [20] Y. Araki, Magnetic textures and dynamics in magnetic weyl semimetals, *Ann. Phys.* **532**, 1900287 (2020).
- [21] Z. Guguchia, J. A. T. Verezhak, D. J. Gawryluk, S. S. Tsirkin, J.-X. Yin, I. Belopolski, H. Zhou, G. Simutis, S.-S. Zhang, T. A. Cochran, G. Chang, E. Pomjakushina, L. Keller, Z. Skrzeczowska, Q. Wang, H. C. Lei, R. Khasanov, A. Amato, S. Jia, T. Neupert, H. Luetkens, and M. Z. Hasan, Tunable anomalous hall conductivity through volume-wise magnetic competition in a topological kagome magnet, *Nat. Commun.* **11**, 559 (2020).
- [22] D. Destraz, L. Das, S. S. Tsirkin, Y. Xu, T. Neupert, J. Chang, A. Schilling, A. G. Grushin, J. Kohlbrecher, L. Keller, P. Puphal, E. Pomjakushina, and J. S. White, Magnetism and anomalous transport in the weyl semimetal PrAlGe : possible route to axial gauge fields, *npj Quantum Mater.* **5**, 5 (2020).
- [23] C. Liu, J. Shen, J. Gao, C. Yi, D. Liu, T. Xie, L. Yang, S. Danilkin, G. Deng, W. Wang, S. Li, Y. Shi, H. Weng, E. Liu, and H. Luo, Spin excitations and spin wave gap in the ferromagnetic weyl semimetal $\text{Co}_3\text{Sn}_2\text{S}_2$, *Sci. China Phys. Mech. Astron.* **64**, 217062 (2021).
- [24] B. Xu, J. Franklin, A. Jayakody, H. Yang, F. Tafti, and I. Sochnikov, Picoscale magnetoelasticity governs heterogeneous magnetic domains in a noncentrosymmetric ferromagnetic weyl semimetal, *Adv. Quantum Technol.* **4**, 2000101 (2021).
- [25] Y. Sun, C. Lee, H.-Y. Yang, D. H. Torchinsky, F. Tafti, and J. Orenstein, Mapping domain-wall topology in the magnetic weyl semimetal CeAlSi , *Phys. Rev. B* **104**, 235119 (2021).
- [26] D. F. Liu, A. J. Liang, E. K. Liu, Q. N. Xu, Y. W. Li, C. Chen, D. Pei, W. J. Shi, S. K. Mo, P. Dudin, T. Kim, C. Cacho, G. Li, Y. Sun, L. X. Yang, Z. K. Liu, S. S. P. Parkin, C. Felser, and Y. L. Chen, Magnetic weyl semimetal phase in a kagomé crystal, *Science* **365**, 1282 (2019).
- [27] S. Sorn and A. Paramekanti, Domain wall skew scattering in ferromagnetic weyl metals, *Phys. Rev. B* **103**, 104413 (2021).
- [28] W. Schnelle, A. Leithe-Jasper, H. Rosner, F. M. Schappacher, R. Pöttgen, F. Pielhofer, and R. Wehlich, Ferromagnetic ordering and half-metallic state of $\text{Sn}_2\text{Co}_3\text{S}_2$, *Phys. Rev. B* **88**, 144404 (2013).
- [29] J. Shen, Q. Zeng, S. Zhang, W. Tong, L. Ling, C. Xi, Z. Wang, E. Liu, W. Wang, G. Wu, and B. Shen, On the anisotropies of magnetization and electronic transport of magnetic weyl semimetal $\text{Co}_3\text{Sn}_2\text{S}_2$, *Appl. Phys. Lett.* **115**, 212403 (2019).
- [30] Y. Okamura, S. Minami, Y. Kato, Y. Fujishiro, Y. Kaneko, J. Ikeda, J. Muramoto, R. Kaneko, K. Ueda, V. Kocsis, N. Kanazawa, Y. Taguchi, T. Koretsune, K. Fujiwara, A. Tsukazaki, R. Arita, Y. Tokura, and Y. Takahashi, Giant magneto-optical responses in magnetic weyl semimetal $\text{Co}_3\text{Sn}_2\text{S}_2$, *Nat. Commun.* **11**, 4619 (2020).
- [31] K. Geishendorf, R. Schlitz, P. Vir, C. Shekhar, C. Felser, K. Nielsch, S. T. B. Goennenwein, and A. Thomas, Magnetoresistance and Anomalous Hall Effect in Micro-Ribbons of the Magnetic Weyl Semimetal $\text{Co}_3\text{Sn}_2\text{S}_2$, *Appl. Phys. Lett.* **114**, 092403 (2019).
- [32] K. Geishendorf, P. Vir, C. Shekhar, C. Felser, J. I. Facio, J. Van Den Brink, K. Nielsch, A. Thomas, and S. T. B. Goennenwein, Signatures of the magnetic entropy in the thermopower signals in nanoribbons of the magnetic weyl semimetal $\text{Co}_3\text{Sn}_2\text{S}_2$, *Nano Lett.* **20**, 300 (2020).
- [33] M. Tanaka, Y. Fujishiro, M. Mogi, Y. Kaneko, T. Yokosawa, N. Kanazawa, S. Minami, T. Koretsune, R. Arita, S. Tarucha, M. Yamamoto, and Y. Tokura, Topological kagome magnet $\text{Co}_3\text{Sn}_2\text{S}_2$ thin flakes with high electron mobility and large anomalous hall effect, *Nano Lett.* **20**, 7476 (2020).
- [34] S.-Y. Yang, J. Noky, J. Gayles, F. K. Dejene, Y. Sun, M. Dörr, Y. Skourski, C. Felser, M. N. Ali, E. Liu, and S. S. P. Parkin, Field-Modulated anomalous hall conductivity and planar hall effect in $\text{Co}_3\text{Sn}_2\text{S}_2$ nanoflakes, *Nano Lett.* **20**, 7860 (2020).
- [35] S. Li, G. Gu, E. Liu, P. Cheng, B. Feng, Y. Li, L. Chen, and K. Wu, Epitaxial growth and transport properties of magnetic weyl semimetal $\text{Co}_3\text{Sn}_2\text{S}_2$ thin films, *ACS Appl. Electron. Mater.* **2**, 126 (2020).
- [36] M. A. Kassem, Y. Tabata, T. Waki, and H. Nakamura, Single crystal growth and characterization of kagomé-lattice shandites $\text{Co}_3\text{Sn}_{2-x}\text{In}_x\text{S}_2$, *J. Cryst. Growth* **426**, 208 (2015).
- [37] M. A. Kassem, Y. Tabata, T. Waki, and H. Nakamura, Structure and magnetic properties of flux grown single crystals of $\text{Co}_{3-x}\text{Fe}_x\text{Sn}_2\text{S}_2$ shandites, *J. Solid State Chem.* **233**, 8 (2016).
- [38] See Supplemental Material at <http://link.aps.org/supplemental/10.1103/PhysRevB.105.144423> for additional experimental details and discussion such as movies of protocols present in the manuscript, magnetotransport, optical, and EDX measurements, and information on the SOT parameters.
- [39] B. D. Cullity and C. D. Graham, Definitions and units, definitions and units, in *Introduction to Magnetic Materials* (John Wiley & Sons, Inc., Hoboken, NJ, 2008), pp. 1–21.
- [40] Y. W. Windsor, A. Gerber, and M. Karpovski, Dynamics of successive minor hysteresis loops, *Phys. Rev. B* **85**, 064409 (2012).
- [41] Y. W. Windsor, A. Gerber, I. Y. Korenblit, and M. Karpovski, Time dependence of magnetization reversal when beginning with pre-existing nucleation sites, *J. Appl. Phys.* **113**, 223902 (2013).
- [42] Y. Cao, K. Xu, W. Jiang, T. Droubay, P. Ramuhalli, D. Edwards, B. R. Johnson, and J. McCloy, Hysteresis in single and polycrystalline iron thin films: major and minor loops, first order reversal curves, and preisach modeling, *J. Magn. Magn. Mater.* **395**, 361 (2015).
- [43] A. Uri, Y. Kim, K. Bagani, C. K. Lewandowski, S. Grover, N. Auerbach, E. O. Lachman, Y. Myasoedov, T. Taniguchi, K. Watanabe, J. Smet, and E. Zeldov, Nanoscale imaging of equilibrium quantum hall edge currents and of the magnetic monopole response in graphene, *Nat. Phys.* **16**, 164 (2020).
- [44] A. Uri, S. Grover, Y. Cao, J. A. Crosse, K. Bagani, D. Rodan-Legrain, Y. Myasoedov, K. Watanabe, T. Taniguchi, P. Moon, M. Koshino, P. Jarillo-Herrero, and E. Zeldov, Mapping the twist-angle disorder and landau levels in magic-angle graphene, *Nature (London)* **581**, 47 (2020).
- [45] D. Vasyukov, Y. Anahory, L. Embon, D. Halbertal, J. Cuppens, L. Neeman, A. Finkler, Y. Segev, Y. Myasoedov, M. L. Rappaport, M. E. Huber, and E. Zeldov, A scanning superconducting quantum interference device with single electron spin sensitivity, *Nat. Nanotechnol.* **8**, 639 (2013).

- [46] Y. Anahory, H. R. Naren, E. O. Lachman, S. Buhbut Sinai, A. Uri, L. Embon, E. Yaakobi, Y. Myasoedov, M. E. Huber, R. Klajn, and E. Zeldov, SQUID-on-Tip with single-electron spin sensitivity for high-field and ultra-low temperature nanomagnetic imaging, *Nanoscale* **12**, 3174 (2020).
- [47] S. Howlader, R. Ramachandran, Y. Singh, and G. Sheet, Domain structure evolution in the ferromagnetic kagome-lattice weyl semimetal $\text{Co}_3\text{Sn}_2\text{S}_2$, *J. Phys.: Condens. Matter* **33**, 075801 (2021).
- [48] C. Lee, P. Vir, K. Manna, C. Shekhar, J. E. Moore, M. A. Kastner, C. Felser, and J. Orenstein, Observation of a Phase Transition within the Domain Walls of the Magnetic Weyl Semimetal $\text{Co}_3\text{Sn}_2\text{S}_2$, [arXiv:2104.13381](https://arxiv.org/abs/2104.13381).
- [49] A. Fernández-Pacheco, E. Vedmedenko, F. Ummelen, R. Mansell, D. Petit, and R. P. Cowburn, Symmetry-Breaking interlayer dzyaloshinskii–moriya interactions in synthetic anti-ferromagnets, *Nat. Mater.* **18**, 679 (2019).
- [50] X. Li, C. Collignon, L. Xu, H. Zuo, A. Cavanna, U. Gennser, D. Mailly, B. Fauqué, L. Balents, Z. Zhu, and K. Behnia, Chiral domain walls of Mn_3Sn and their memory, *Nat. Commun.* **10**, 3021 (2019).
- [51] T. Moriya, Anisotropic superexchange interaction and weak ferromagnetism, *Phys. Rev.* **120**, 91 (1960).